2011

Rotation and Alignment of Rods in Two-Dimensional Chaotic Flow

Shima Parsa

Jeffrey S. Guasto
Haverford College

Monica Kishore '09
Class of 2009, Haverford College

Jerry P. Gollub
Haverford College

AIP | Physics of Fluids

Rotation and alignment of rods in two-dimensional chaotic flow

Shima Parsa, Jeffrey S. Guasto, Monica Kishore, Nicholas T. Ouellette, J. P. Gollub et al.

Citation: Phys. Fluids **23**, 043302 (2011); doi: 10.1063/1.3570526
View online: http://dx.doi.org/10.1063/1.3570526
View Table of Contents: http://pof.aip.org/resource/1/PHFLE6/v23/i4
Published by the American Institute of Physics.

Rotation and alignment of rods in two-dimensional chaotic flow

Shima Parsa,[1] Jeffrey S. Guasto,[2] Monica Kishore,[2] Nicholas T. Ouellette,[3] J. P. Gollub,[2] and Greg A. Voth[1]
[1]*Department of Physics, Wesleyan University, Middletown, Connecticut 06459, USA*
[2]*Department of Physics, Haverford College, Haverford, Pennsylvania 19041, USA*
[3]*Department of Mechanical Engineering and Materials Science, Yale University, New Haven, Connecticut 06520, USA*

(Received 21 May 2010; accepted 4 March 2011; published online 21 April 2011)

We study the dynamics of rod shaped particles in two-dimensional electromagnetically driven fluid flows. Two separate types of flows that exhibit chaotic mixing are compared: one with time-periodic flow and the other with constant forcing but nonperiodic flow. Video particle tracking is used to make accurate simultaneous measurements of the motion and orientation of rods along with the carrier fluid velocity field. These measurements allow a detailed comparison of the motion and orientation of rods with properties of the carrier flow. Measured rod rotation rates are in agreement with predictions for ellipsoidal particles based on the measured velocity gradients at the center of the rods. There is little dependence on length for the rods we studied (up to 53% of the length scale of the forcing). Rods are found to align weakly with the extensional direction of the strain-rate tensor. However, the alignment is much stronger with the direction of Lagrangian stretching defined by the eigenvectors of the Cauchy–Green deformation tensor. A simple model of the stretching process predicts the degree of alignment of rods with the stretching direction. © *2011 American Institute of Physics*. [doi:10.1063/1.3570526]

I. INTRODUCTION

The transport of particulate material by fluids is a problem with far-reaching consequences, and thus a long history of study. When the particles are very small and neutrally buoyant, they tend to act as Lagrangian tracers and move with the local fluid velocity. Particles with a density greater than or less than the carrier fluid, however, tend to show different dynamics, such as preferential concentration and clustering in turbulent flow fields.[1] Even particles that are neutrally buoyant can show dynamics different from the underlying flow when they are large compared to the smallest flow scales, since they filter the flow field in complex ways.[2–4] A large number of papers on particle transport have focused on the case of spherical particles. In many situations, however, including fiber processing in the paper industry[5] and dynamics of ice in clouds,[6–9] the particles are not round. The case of ellipsoidal particles was first studied by Jeffery[10] and Taylor;[11] subsequently, Brenner addressed the case of general particle shape in a series of seminal papers.[12–15]

Here, we study the motion of rod-like particles experimentally in quasi-two-dimensional flow. We focus on the rotational dynamics, since we expect that spheres and rods will rotate in qualitatively different fashions. As long as the Reynolds number at the particle scale is small (so that the local flow is well approximated by a Stokes flow), spheres will rotate with an angular velocity $\dot{\theta}$ given by half the flow vorticity ω. An anisotropic particle, however, will also couple with the strain-rate. In a two-dimensional (2D) Stokes flow with uniform velocity gradients, the rotation rate of an ellipsoid is given by[5,12–15]

$$\dot{\theta} = \frac{1}{2}\left[\omega + \left(\frac{1-\alpha^2}{1+\alpha^2}\right)\left[\sin(2\theta)\left(\frac{\partial u_x}{\partial x} - \frac{\partial u_y}{\partial y}\right) - \cos(2\theta) \times \left(\frac{\partial u_y}{\partial x} + \frac{\partial u_x}{\partial y}\right)\right]\right], \quad (1)$$

where θ is the inclination of the rod with respect to a fixed axis, α is the aspect ratio of the ellipsoid, and u is the fluid velocity. If the velocity gradient changes in space, Eq. (1) is still the first term in a series expansion in higher spatial derivatives of the velocity. The coefficient of the strain-rate portion of the equation is the eccentricity of the ellipsoid, and is constrained to lie between zero (for spheres) and one (for lines). Even though the right circular cylinders we study have sharp corners when compared with ideal ellipsoids, we expect any correction terms to Eq. (1) to be negligible at this order of approximation, and our measurements confirm this.

These insights about how rods couple to strain-rate and vorticity have been extended in many different directions by recent work. Analytic studies of rod motion in flows with uniform velocity gradients have explored Jeffery orbits and deviations from them due to walls and fluid inertia.[16,17] Szeri *et al.*[18–21] developed analytical techniques to identify pattern formation in the orientation distribution of suspended microstructures in simple flows. In the more complex chaotic flows of interest here, the orientation dynamics become nonintegrable and the velocity gradients often change appreciably over the length of a particle. Models of the dynamics of thin rods in turbulent flows have been developed;[5] however, instantaneous flow fields are required to determine rod trajectories. In the limit of small rods with high aspect ratio, the rods approximate material lines, and one can use theoretical techniques developed for studying the evolution of material

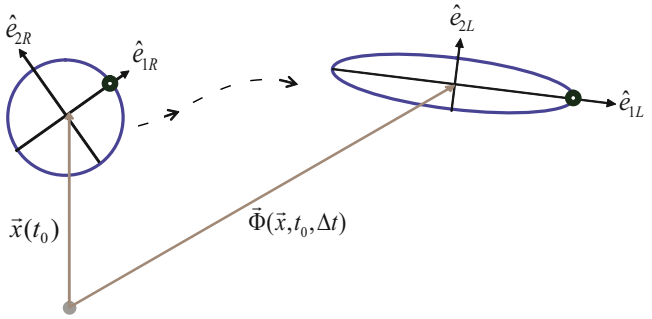

FIG. 1. (Color online) A fluid element at initial position $\vec{x}$ at time t_0 is mapped to final position $\vec{\Phi}$ after time Δt by the flow. The circular fluid element is also deformed by the flow to an ellipse. The eigenvectors of the left ($\hat{e}_{1L}$ and $\hat{e}_{2L}$) and right ($\hat{e}_{1R}$ and $\hat{e}_{2R}$) Cauchy–Green tensors are shown.

lines in turbulence[22,23] to study the motion of rods.

Numerical simulations provide access to the motion of the particles along with the velocity of the carrier flow and allow detailed study of the motion of particles in complex flows;[24–27] however, they must either use a drag model for the particle fluid interactions or fully resolve the particle boundary layer. Experimental studies have not been able to access both rod motion and the full fluid velocity field in flows more complex than uniform velocity gradients. Several groups have studied orientation dynamics in flows with uniform velocity gradients, where the effects of inertia,[28] aspect ratio, and distance from solid boundaries[29,30] have been investigated. In more complex flows, the rotational diffusivity[31] and orientation distribution in laboratory coordinates[32,33] have been measured.

In our experiments, we have access to high-resolution time-dependent velocity fields, allowing us to characterize both the Lagrangian and Eulerian flow dynamics. We can therefore directly compare the orientation of the rods with properties of the carrier flow. Below, we first study the alignment of rods with the strain-rate tensor ($s_{ij}=1/2[\partial u_i/\partial x_j + \partial u_j/\partial x_i]$) measured at the position of the rod, and subsequently consider alignment with the Lagrangian history of the velocity gradients, defined by the Cauchy–Green deformation tensors.

To quantify the Cauchy–Green deformation tensors, we use the flow map $\vec{\Phi}(\vec{x},t_0,\Delta t)$, which specifies the position at time $t_0+\Delta t$ of a fluid element that was located at position $\vec{x}$ at time t_0; see Fig. 1. The deformation gradient tensor $F_{ij}=(\partial\Phi_i/\partial x_j)$ characterizes the deformation of a fluid element by the flow map. Since F_{ij} is not necessarily symmetric, its eigenvalues may not be purely real. We therefore use the left and right Cauchy–Green deformation tensors,[34] which are the two possible symmetric inner products of F_{ij} with itself,

$$C_{ij}^{(L)} = FF^T = \frac{\partial\Phi_i}{\partial x_k}\frac{\partial\Phi_j}{\partial x_k}, \tag{2a}$$

$$C_{ij}^{(R)} = F^TF = \frac{\partial\Phi_k}{\partial x_i}\frac{\partial\Phi_k}{\partial x_j}. \tag{2b}$$

The eigenvalues of $C_{ij}^{(L)}$ are the same as the eigenvalues of $C_{ij}^{(R)}$, which are real and positive. The square root of the maximum eigenvalue gives the stretching that the fluid element has experienced over the time Δt. To visualize this process, consider a fluid element that is initially circular and is stretched into an ellipse by the flow, as in Fig. 1. The stretching is the ratio of the semimajor axis of the ellipse to the radius of the circle. The spatial distribution of stretching in fluid flows is closely related to the finite time Lyapunov exponents, and is used to define Lagrangian coherent structures.[35–38]

Even though the eigen*values* of the two Cauchy–Green tensors are identical, the eigen*vectors* are in general not parallel. As shown in Fig. 1, the eigenvectors of the left Cauchy–Green tensor, $C_{ij}^{(L)}$, indicate the direction of stretching in a coordinate system aligned with the fluid element at time $t_0+\Delta t$, so that the eigenvectors give the directions of the principal axes of the ellipse after stretching. The eigenvectors of the right Cauchy–Green tensor, $C_{ij}^{(R)}$, on the other hand, indicate the direction of stretching in a coordinate system aligned with the fluid element at time t_0, so that material lines initially aligned with the right eigenvectors will end up aligned with one of the principal axes of the ellipse after stretching. We will denote the eigenvector corresponding to the maximum (extensional) eigenvalue of the right Cauchy–Green deformation tensor as $\hat{e}_{1R}$, and the left Cauchy–Green tensor as $\hat{e}_{1L}$.

This method is somewhat different from methods used by Szeri *et al.*[20,21] and Wilkinson *et al.*[27] in their extensive analysis of the patterns formed by the orientation of rods advected in fluid flows. They compared the orientation of rods with the direction defined by the eigenvector of the deformation gradient tensor. As mentioned earlier, the eigenvalues of this tensor may be complex numbers in contrast to the eigenvalues of the Cauchy–Green deformation tensor. In simulations of random flow,[27] it has been shown that rods will be asymptotically oriented in the direction of the eigenvector corresponding with the largest eigenvalue of the deformation gradient tensor. They also show that regions of complex eigenvalues exist at short times, but disappear at longer integration times. We find the method based on the Cauchy–Green deformation tensors to be more useful for analysis of the experimental trajectories that are limited to relatively short times (typically a few inverse Lyapunov exponents), where the deformation gradient often has complex eigenvalues.

In the remainder of this paper, we present the results of two sets of experiments that measured both the rod motion and the fluid velocity field that advected the rods. We first show that the rotation rates of the rods are well described by Eq. (1). Next, we consider the alignment of rods with the strain-rate and the Lagrangian stretching, and find that rods align more strongly with the stretching. Finally, we develop a simple model of the degree of alignment of rods with the stretching experienced by the fluid.

II. EXPERIMENTAL METHODS

We study the motion of anisotropic particles (right circular cylinders) in chaotic quasi-two-dimensional fluid flows, where time-periodic and nonperiodic flows are considered.

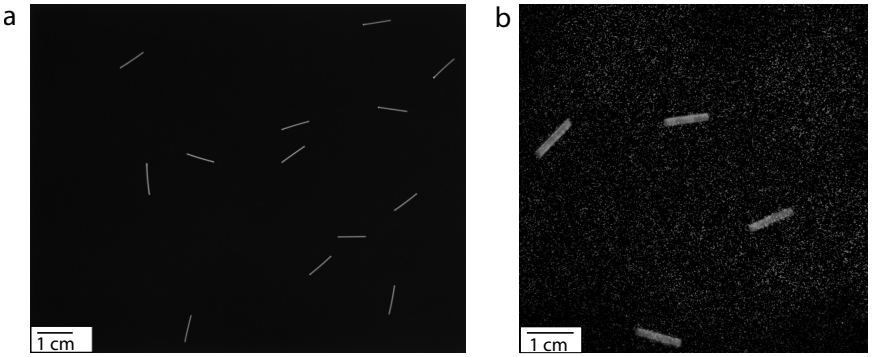

FIG. 2. (a) Raw image of 10 mm rods in the periodic flow; (b) raw image of 10 mm rods along with tracer particles in the nonperiodic flow.

The flows are produced in a shallow electrolytic fluid layer that is driven electromagnetically using Lorentz forcing.[36] A current (sinusoidal or constant) flows through the fluid layer, which interacts with the magnetic field provided by an arrangement of permanent magnets located beneath the plane of the fluid. This results in a body force on the fluid perpendicular to both the current and magnetic field. The Reynolds number is defined as $\mathrm{Re}=UL/\nu$, where U is the root mean square fluid velocity, L is the forcing length scale given by the typical magnet spacing, and ν is the kinematic viscosity of the fluid. In both types of flows, Re was moderate ($95 \leq \mathrm{Re} \leq 187$), but somewhat smaller in the periodic case ($\mathrm{Re}=95$).

The periodic and nonperiodic flows were measured in separate but similar apparatuses.[39] In both cases, we use particle tracking methods to determine the trajectories and orientations of the rods. The time-resolved fluid velocity fields are also measured by tracking the motion of small tracer particles advected by the flow. Unlike the time-periodic flow, characterization of the rod and fluid motion must be performed simultaneously in the nonperiodic case. This presents some interesting technical challenges described briefly below and in detail elsewhere.[3] The electrolyte solutions are chosen to provide electrical conductivity and to render the rods and tracer particles neutrally buoyant, which ensures that they coincide in a single plane of the fluid.

A. Experimental setup: Periodic flow

For the time-periodic flow, the fluid density ($\rho=1.22$ g/cm^3, 30% $CaCl_2$ in water) is 1.6% higher than the rods ($\rho=1.20$ g/cm^3), so that the rods float at the upper surface. The rods are made from fluorescent plastic fiber optic cable (0.5 mm diameter) that is cut to the desired length (2.5–10 mm).

The same material is used to make tracer particles (0.5 mm long cylinders), which ensures that the tracers and rods float at the same height in the fluid. Ultraviolet lamps are used for fluorescence excitation. A random arrangement of permanent magnets with an average spacing of $L=1.9$ cm is located beneath the shallow fluid layer (1.7 mm deep, 21×21 cm wide). A sinusoidal electric current, with frequency 0.1 Hz (period $T=10$ s), travels horizontally through the fluid, which leads to a time-periodic chaotic flow ($\mathrm{Re}=95$, $U=0.91$ cm/s).

B. Image analysis: Periodic flow

We image a 16×13 cm^2 (1280×1024 pixels^2) area in the center of the test section to avoid edge effects. Figure 2(a) shows a typical raw image of 10 mm rods taken at a frame rate of 40 Hz. Since the flow is time-periodic, the fluid velocity can be measured separately without the rods present.

For measurement of the fluid velocity field, the flow is seeded with tracer particles to an average concentration of 230 particles per image, and their motion is tracked over 115 periods resulting in about 27 000 tracer particles per phase. The center of each tracer particle is measured with an uncertainty less than ≈ 30 μm (0.25 pixel). The particle velocities are measured by fitting a polynomial to the particle trajectories. The fluid velocity field is then extracted from all the tracer velocities occurring at the same phase by interpolation onto a square grid of 0.1 cm spacing.

In separate experiments, the rod motion is measured with a significantly lower particle concentration (10–40 depending on rod length) to avoid particle-particle interactions, and repeated 70–90 periods for each rod length. To determine the center and orientation of each rod, we find all bright pixels corresponding to a single rod. The rod position is determined using the intensity-weighted center-of-mass of the pixels. A Hough transform gives a first guess for the orientation of the rod. Finally, we use a nonlinear fitting algorithm to optimize the orientation measurements by minimizing the difference between an ideal model rod image and the raw image. Using this method, the orientation of a rod is found to within ± 0.017 rad accuracy.

C. Experimental setup: Nonperiodic flow

For chaotic nonperiodic flows, it is necessary to measure the fluid motion simultaneously with the rod dynamics. To achieve this, tracer particles are seeded along with the rods at the interface of a density stratified fluid bilayer.[3] The lower layer is a dense electrolytic solution (17% KCl in water, $\rho=1.11$ g/cm^3), the upper fluid layer is deionized water, and the tracers and rods have an intermediate density ($\rho_p=1.05$ g/cm^3). Surface tension interactions between the particles are eliminated, since the upper and lower fluids are miscible.[40] This allows for much higher tracer seeding as compared to particle seeding at a free surface. The tracer particles (80 μm diameter) are significantly smaller than the

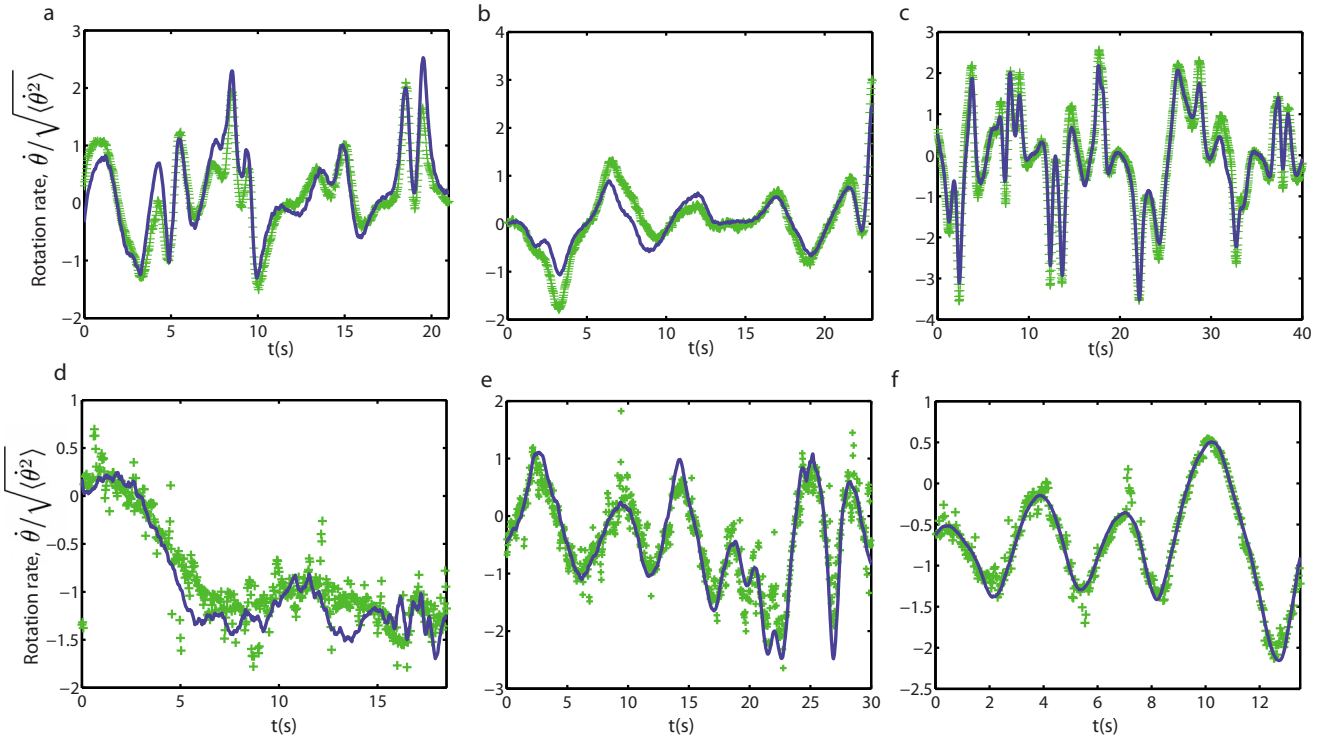

FIG. 3. (Color online) Measured (solid line) and predicted (+) rotation rate vs time for different rod lengths {[(a), (d)] 2.5 mm, [(b), (e)] 5 mm, [(c), (f)] 10 mm} in periodic flow (top row) and nonperiodic flow (bottom row).

rods (1.59 mm diameter, 2.5–10.0 mm long) to achieve sufficient resolution of the fluid velocity field in the vicinity of a rod.

The fluid layers are each 3.5 mm deep with an area 21 $\times 20$ cm^2, and a constant current is maintained through the layer to drive the flow. The magnets are arranged in a square lattice with alternating poles and a spacing $L=2.54$ cm. When driven at a sufficiently high current, the resulting flow is spatiotemporally chaotic with a Reynolds number in the range $139 \leq \mathrm{Re} \leq 187$.

D. Image analysis: Nonperiodic flow

To avoid edge effects, we image an $\sim 8.0 \times 8.0$ cm^2 (600×600 pixels^2) region of interest in the center of the flow cell at a frame rate of 30 Hz. The tracer particles are imaged using fluorescence, and scattered light is used to image the much larger rods. Each image contains >15 000 tracers to adequately resolve the flow field, while the rods are much fewer in number (<10 per image) to avoid particle-particle interactions.

Figure 2(b) shows a raw image of 10 mm rods along with the tracer particles, where rods are easily distinguished from tracers by size. The center and orientation of each rod are identified by an intensity-weighted moment yielding the centroid and principal axes of the rod. Tracer particle centers are detected with subpixel accuracy (≈ 13 μm) by Gaussian fitting to their diffraction limited images. Both sets of particles are tracked using a predictive algorithm,[41] where instantaneous particle velocities (and angular velocities) are measured by polynomial fitting to the trajectories. The tracer particle velocities are bilinearly interpolated to further resolve the fluid velocity in the vicinity of each rod (see Ref. 3 for additional details). This method provides the distinct advantage of direct measurement of the fluid velocity field simultaneously with the anisotropic particle dynamics, which is essential for nonperiodic flows.

III. RESULTS

A. Rotation rate

Equation (1) shows that the rotation rate of a rod in two dimensions can be estimated from the carrier fluid velocity gradient at the center of the rod. Figure 3 shows the measured rotation rate of several typical rods of different lengths. Also shown is the predicted rotation rate from Eq. (1) using experimentally measured velocity gradients at the position of the rod. The top row data [(a)–(c)] are selected from the periodic flow and the bottom row [(d)–(f)] are selected from the nonperiodic flow experiment. Rod length increases from left to right. We measure the rotation rate of the rods from polynomial fits to the experimentally measured orientations.

As shown in Fig. 3, the predicted rotation rate is close to the experimentally measured rotation rate for all rod lengths we have studied. This may be surprising since our rods have lengths up to 53% of the length scale of the forcing and particle Reynolds numbers up to 74 (based on the rod length and the rms fluid velocity). Equation (1) gives good predictions despite the fact that the particles do not rigorously satisfy the conditions for which it was derived. The significantly larger noise in the data for a 2.5 mm rod in the nonperiodic flow [Fig. 3(d)] is mostly generated by inaccuracy in determining the exact orientation of short rods. Also, difficulties

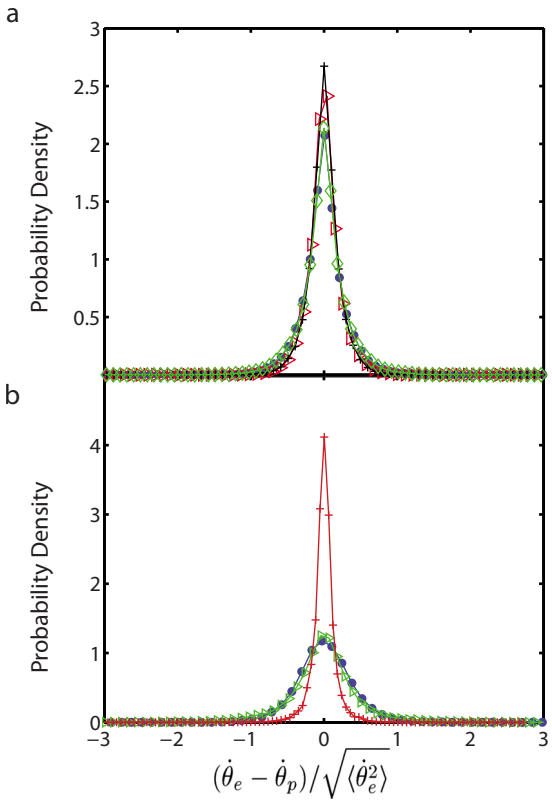

FIG. 4. (Color online) Probability density function (PDF) of the differences between measured and predicted rotation rates for different rod lengths in both sets of experiments: (a) Periodic flow, rod lengths are: ● 2.5 mm, ▷ 5 mm, + 7.5 mm, ◇ 10 mm; (b) nonperiodic flow, rod lengths are: ● 2.5 mm, ▷ 5 mm, + 10 mm.

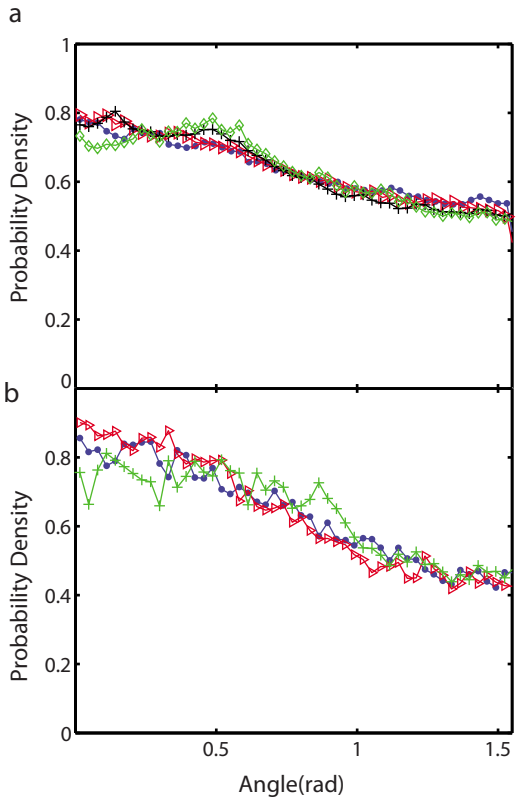

FIG. 5. (Color online) Probability density function (PDF) of the angles between rod orientation and extensional direction of strain-rate. In both experiments, the PDF shows weak alignment of rods with the strain-rate. (a) Periodic flow, rod lengths are: ● 2.5 mm, ▷ 5 mm, + 7.5 mm, ◇ 10 mm; (b) nonperiodic, rod lengths are: ● 2.5 mm, ▷ 5 mm, + 10 mm.

in measuring the velocity gradients in real time contribute to inaccuracies in the predicted rotation rate. The probability distribution of the deviation between the predicted rotation rate and the experimentally measured rotation rate is shown in Fig. 4. For the periodic flow in Fig. 4(a), the deviations of the prediction from measurement are about 20% of the root mean square rotation rate, and are mostly independent of rod length. The major contribution to these deviations is inaccuracy in determining the exact velocity gradient of the flow at the center of the rod. The probability distribution in Fig. 4(b) shows that for 10 mm rods in the nonperiodic flow, the prediction is much closer to the measurement than it is for shorter rods. The smaller deviation for the long rods is the result of the smaller uncertainty in determining the orientation of the longer rods.

B. Alignment of rods with strain-rate

The orientation distribution of rods can be considered relative to different directions defined by the flow. First, we will consider alignment with the local strain-rate. Figure 5 shows the probability distribution of angles between the orientation of rods and the extensional direction of the strain-rate calculated at the center of the rods. This distribution shows that the rods tend to align with the extensional direction of the strain-rate, although the alignment is fairly weak. For the rods studied, the alignment with the strain-rate does not show significant dependence on rod length.

C. Alignment of rods with stretching

Rods are weakly aligned with the strain-rate in these flows, but it is really the history of the velocity gradients along the trajectory of a rod that is responsible for its orientation distribution. As discussed in the introduction, this Lagrangian history of the velocity gradients can be quantified using the Cauchy–Green deformation tensors. In Fig. 6, we show snapshots of the past stretching field, defined by the eigenvalue of the Cauchy–Green deformation tensor at each spatial point. In both the periodic and nonperiodic flows, the stretching field has many sharp maxima that are organized into lines. Superimposed on the stretching fields in Fig. 6, we show images of 10 mm rods taken at the same time. Animations of rod motion in time-dependent stretching fields are available in the enhanced online version of Fig. 6.

The rods are preferentially aligned with the stretching lines, which indicates the important role of stretching in orienting rods. As in Ref. 36, we calculate stretching by integrating trajectories of virtual particles in measured velocity fields. The gradients in the definition of the Cauchy–Green tensors Eq. (2) are evaluated using finite differences of particle trajectories that are initially very close to each other. A rescaling method is used to keep the particles close to each other even as they experience exponential stretching.

In order to quantify the effect of stretching on the orientation of rods, we measure the distribution of angles between the orientation of each rod and the direction of past stretch-

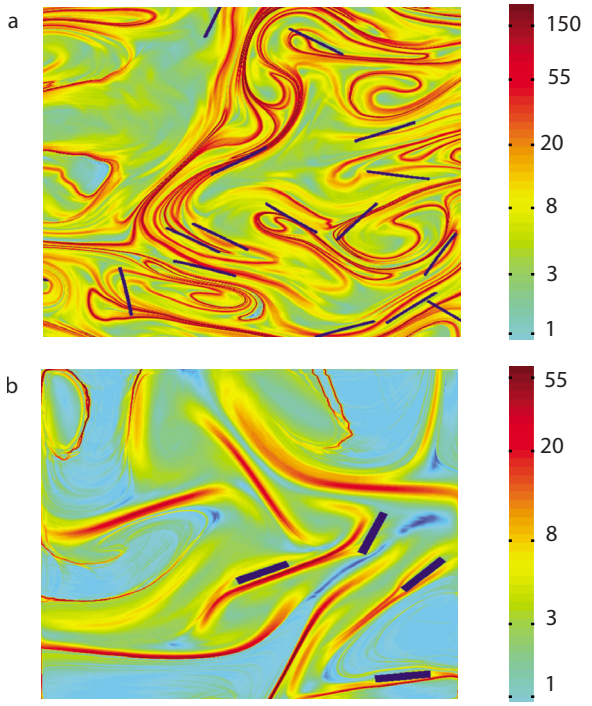

FIG. 6. (Color online) Stretching fields with 10 mm rods superimposed in dark color. (a) Periodic flow with $\Delta t=T=10$ s. (b) Nonperiodic flow with $\Delta t=L/U=4$ s. (enhanced online) [URL: http://dx.doi.org/10.1063/1.3570526.1] [URL: http://dx.doi.org/10.1063/1.3570526.2].

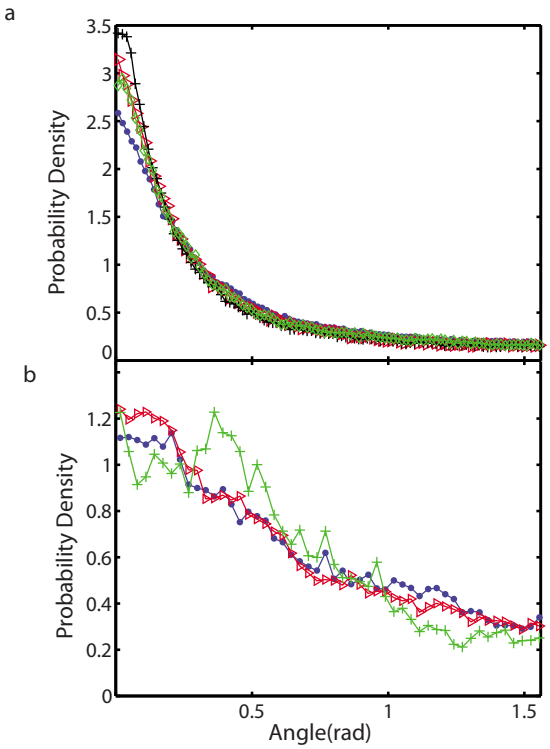

FIG. 7. (Color online) PDF of the alignment of rods with the direction of stretching defined by $\hat{e}_{1L}$. In both sets of experiments, all rod lengths align with the stretching direction. (a) Periodic flow, $\Delta t=T$, rod lengths are: ● 2.5 mm, ▷ 5 mm, + 7.5 mm, ◇ 10 mm; (b) nonperiodic flow, $\Delta t=L/U$, rod lengths are: ● 2.5 mm, ▷ 5 mm, + 10 mm.

ing, $\hat{e}_{1L}$, at the center of the rod. Figure 7 shows that this distribution has large probability around zero, indicating that the rods preferentially align with the past stretching direction. The alignment is significantly stronger than the alignment with the strain-rate direction in Fig. 5. Surprisingly, the alignment is nearly independent of rod length even though the longest rods (10 mm) are 53% of the magnet spacing in the periodic flow experiment and 40% of the magnet spacing in the nonperiodic flow experiment. Even for these relatively large rods, there is no measurable effect either from the rods averaging over the spatially varying velocity field or from the rotational inertia of the rods. The alignment in the periodic flow is stronger than in the nonperiodic flow. This may be partly a result of periodicity, but it is also affected by the larger stretching in the periodic flow for the integration times chosen. Figure 8 shows the probability distribution of alignment of rods with the direction of past stretching for different integration times. The probability of alignment of rods with the direction of stretching increases with increasing integration time. This increase in alignment seems natural, as the bit of fluid that is accompanying the rod after longer integration has experienced more stretching. However, at some point the maximum probability saturates so that further increases in the integration time do not lead to additional alignment. This saturation may be a sign of limitations on the accuracy of the experimental measurements of the stretching direction of the fluid at the center of the rod. (See appendix)

We have also compared rod orientation in our flows to the direction defined by the eigenvectors of the deformation gradient tensor as used in previous studies.[20,27] Even after two periods (20 s) of the time-periodic flow, there are many

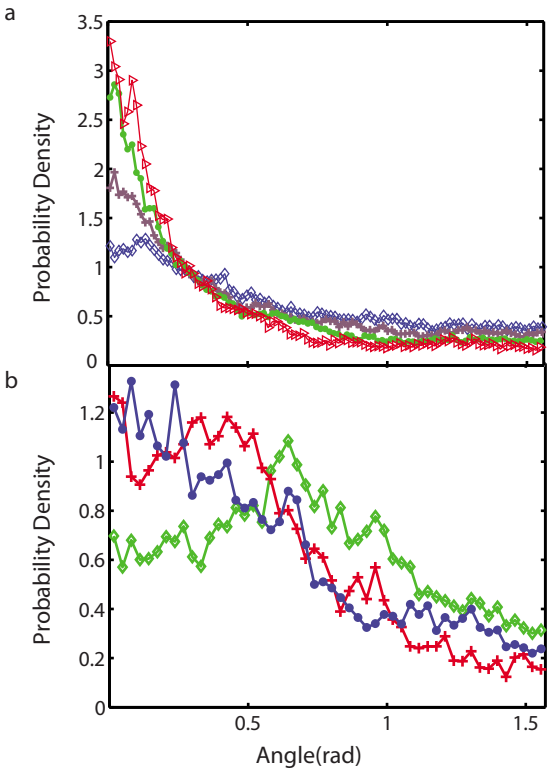

FIG. 8. (Color online) Dependence of stretching alignment on integration time. The PDF of the alignment of rods with the direction of stretching is shown for 10 mm rods with different stretching integration times. Alignment increases for longer integration times. (a) Periodic flow, ($T=10$ s and Lyapunov exponent $0.97T^{-1}$): $\Delta t=$ ◇ $T/16$, + $T/8$, ● $T/4$, ▷ $T/2$; (b) nonperiodic flow, ($L/U=4$ s and Lyapunov exponent $1.03\ U/L$): Δt = ◇ $L/2U$, + L/U, ● $2L/U$.

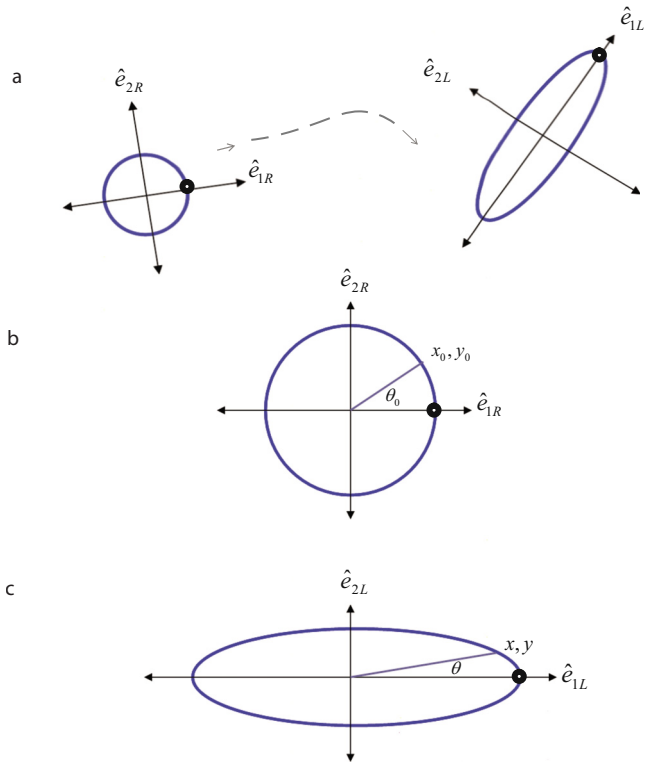

FIG. 9. (Color online) (a) Deformation of a circular fluid element into an ellipse by the flow. (b) Initial circle in the coordinate system aligned with the principal axes of the right Cauchy–Green deformation tensor. (c) Final ellipse in the coordinate system aligned with the principal axes of the left Cauchy–Green deformation tensor.

regions with complex eigenvalues. In these regions, the direction of the eigenvector of the deformation gradient is undefined, so the method based on the Cauchy–Green deformation tensors is more useful for comparing the alignment of rods with the deformation measured in our flows. It would be interesting for future work to make a more detailed comparison of these two methods.

D. Theoretical prediction of alignment of material lines with stretching direction

Here we use a simple model of deformation to predict the alignment of material lines due to stretching in our system. Some theoretical tools for solving the Fokker–Planck equation for the orientation distribution of the microstructure in fluid flows have been developed,[42] but we choose to solve a simple model that clearly reveals the connection of stretching to the orientation distribution. The effect of flow is to deform an infinitesimal circle of fluid into an ellipse. The ratio of the semimajor axis of the ellipse to the radius of the circle is equal to the stretching that the circle has experienced, which can be measured using the square root of the maximum eigenvalue of the Cauchy–Green tensor as described in Sec. III C. If we consider straight material line segments through the center of the circle with a known initial distribution of angles, we can calculate the probability distribution of their angles after being stretched by the flow.

Figure 9(a) shows an initially circular fluid element that is then transported and stretched by the flow into an ellipse. In Fig. 9(b), we show the initial circle in the coordinate system aligned with the principal axes of the right Cauchy–Green tensor. Here, a point on the circle of radius r is given by the simple parametric equations, $x_0 = r\cos(\theta_0)$ and $y_0 = r\sin(\theta_0)$. After deformation by the flow over some time interval, the circle becomes an ellipse with the same area. In general, the flow will have reoriented the ellipse, so in Fig. 9(c) we show the ellipse in the coordinate system defined by the principal axes of the left Cauchy–Green tensor. By choosing different coordinate systems in Figs. 9(b) and 9(c), we have used the Cauchy–Green tensors to account for rotation, leaving only the effect of stretching. We can map any point (x_0, y_0) on the circle to the corresponding point (x, y) on the ellipse by

$$x = sx_0,$$

$$y = \frac{y_0}{s},$$

where s is the stretching.

The angle between the point (x, y) and the semimajor axis of the ellipse is

$$\theta = \arctan\left(\frac{y}{x}\right) = \arctan\left[\frac{\tan(\theta_0)}{s^2}\right]$$

so the final and initial angles of any material line through the center of the material element are related by

$$\tan(\theta) = \frac{1}{s^2}\tan(\theta_0). \tag{3}$$

The number of lines in a range $d\theta$ is given by the number of lines that are mapped to this range from the initial distribution, so the probability distribution of angles, $P(\theta)$, is related to the initial distribution, $P_0(\theta_0)$, by

$$P(\theta)d\theta = P_0(\theta_0)d\theta_0.$$

From Eq. (3), the differentials are related by

$$\frac{d\theta_0}{d\theta} = \frac{d}{d\theta}\{\arctan[s^2\tan(\theta)]\} = \frac{1}{s^2\sin^2(\theta) + \frac{\cos^2(\theta)}{s^2}},$$

so the final distribution of angles in range $d\theta$ for a given value of stretching, s, is

$$P(\theta)d\theta = \frac{P_0\{\arctan[s^2\tan(\theta)]\}d\theta}{s^2\sin^2(\theta) + \frac{\cos^2(\theta)}{s^2}}. \tag{4}$$

Equation (4) implies that the final distribution of angles depends on the initial distribution $P_0(\theta_0)$ and the amount of stretching, s, that the material lines have experienced. If rods rotate as material lines, we can use this theory to predict the final distribution of orientations of rods.

Rods in different regions of the flow experience different values of stretching. The probability distribution of orientations of rods is the sum over all stretching values weighted by the probability density of any particular value of stretching $P(s)$,

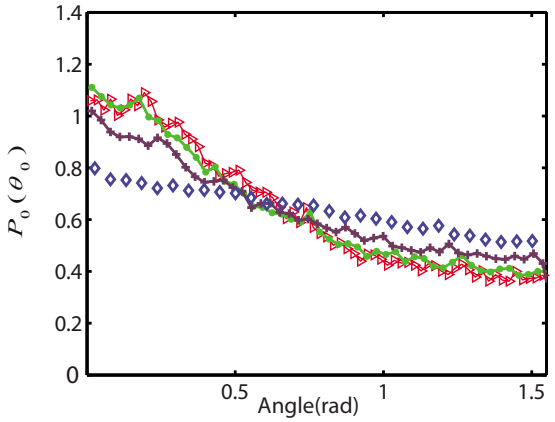

FIG. 10. (Color online) Experimental PDF of initial orientations of rods with respect to the extensional eigenvector of the right Cauchy–Green deformation tensor. Results are shown for 10 mm rods in the periodic flow for four different integration times, $\Delta t = \diamond\ T/16$, $+\ T/8$, $\bullet\ T/4$, $\triangleright\ T/2$. Because the right Cauchy–Green deformation tensor changes with integration time, this distribution has a weak integration time dependence even though the rods always have the same initial orientation.

$$P(\theta)d\theta = \int P(s)ds \frac{P_0\{\arctan[s^2\tan(\theta)]\}d\theta}{s^2\sin(\theta) + \dfrac{\cos^2(\theta)}{s^2}}. \tag{5}$$

The stretching distribution $P(s)$ is measured from all rod positions to account for their sampling of the flow, and we further condition $P_0(\theta_0)$ on values of stretching s.

To compare our measured orientation distributions with the prediction in Eq. (5), we need to know the PDF of initial orientations of rods, $P_0(\theta_0)$. Figure 10 shows this initial probability distribution from our experimental measurements, where θ_0 is the angle between rod orientation and the extensional eigenvector of the right Cauchy–Green deformation tensor, $\hat{e}_{1R}$. Rods show weak alignment with the direction of future stretching, $\hat{e}_{1R}$. One might expect that there would be no alignment with the stretching that the rod will experience in the future, but we find a weak alignment, which can be understood as a result of the time correlation of the velocity gradients of the flow.

From the measured initial distribution of rod orientation in Fig. 10, we can calculate the final probability distribution of orientation of rods using Eq. (5). Figure 11 compares this theoretical prediction of the final distribution of rod orientation with our measurements from the periodic flow (Fig. 8) for four different integration times. Both the predicted and measured distributions give angles measured from the extensional eigenvector of the left Cauchy–Green tensor, $\hat{e}_{1L}$. The predicted distribution shows alignment with the direction of stretching in fairly good agreement with our measurements; however, the theory predicts somewhat stronger alignment than is observed. The deviation is largest for long integration times where the theory predicts that material lines are strongly aligned by the stretching to produce a sharp peak near zero in Fig. 11(d). Inaccuracies in our measured velocity fields may lead to slightly inaccurate measurements of the stretching direction. These inaccuracies would have the largest effect in regions with nearly perfect alignment leading to smaller probability in the experimental distribution near $\theta = 0$. Another factor could be that rods are not material lines. Either their length or aspect ratio could cause the measured alignment to differ from the prediction for material lines. However, the lack of rod length dependence in the alignment distribution (see Fig. 7) suggests that this is not a large effect.

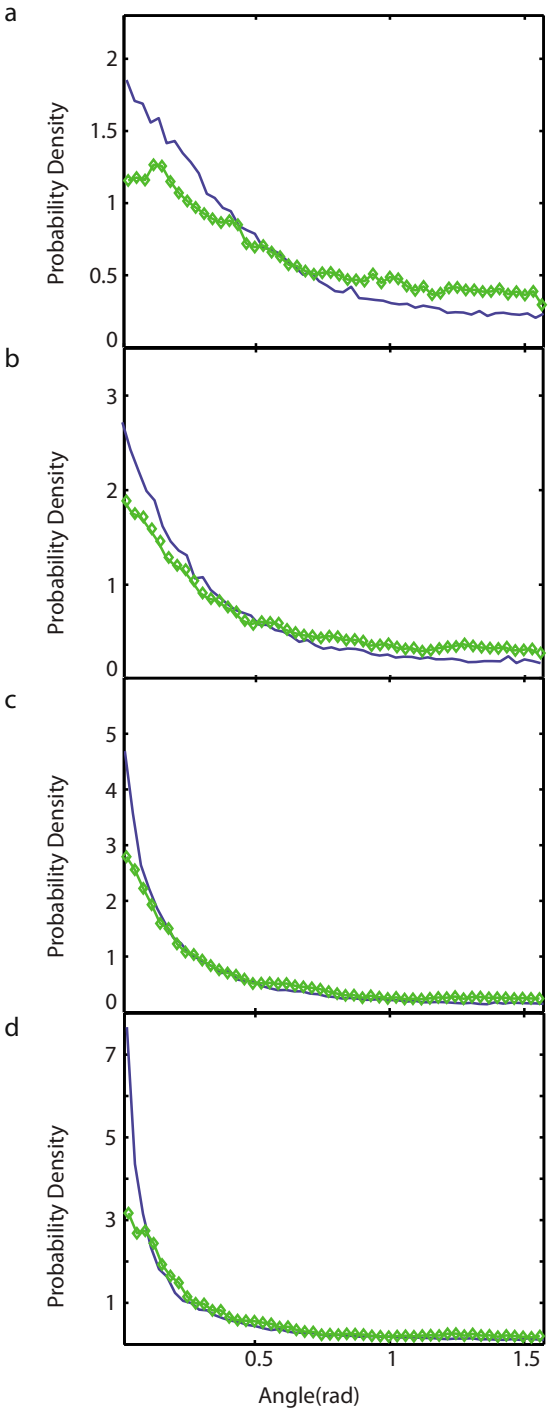

FIG. 11. (Color online) Comparison between the predicted (solid line) and measured ($\diamond$) distribution of rod alignment with the stretching direction. Results are shown for 10 mm rods in the periodic flow for four different integration times, Δt=(a) $T/16$, (b) $T/8$, (c) $T/4$, (d) $T/2$.

IV. CONCLUSIONS

Simultaneous measurements of rod motion and the velocity field advecting the rods provide a powerful new tool for understanding particles in complex flows. We have developed methods for making these measurements in two types of flows: periodic and nonperiodic. Particularly important is the development of techniques for simultaneously extracting the rod and fluid motion in the nonperiodic flow. The measured rotation rates of rods show good agreement with the rotation rate predicted for ellipsoidal particles without inertia in a flow with uniform velocity gradient, even for the longest rods studied.

We find that rods align weakly with the extensional direction of strain-rate; however, the alignment with the eigenvectors of the Cauchy–Green deformation tensor is much stronger. In both periodic and nonperiodic flows, the alignment of rods with the direction of the Cauchy–Green deformation tensor is almost independent of rod length, even though the rods extend to 53% of periodic flow length scale and 40% of nonperiodic flow length scale. We developed a simple model to predict the alignment of rods with the direction of stretching based on the assumption that rods rotate as material lines. The model captures the main features of the alignment distributions, but predicts a slightly stronger alignment than the experimental measurements show.

ACKNOWLEDGMENTS

We thank Bruce Boyes for technical assistance. This work was supported by NSF Grant Nos. DMR-0803153 to Haverford College and DMR-0547712 to Wesleyan University.

APPENDIX: EFFECTS OF DEVIATIONS BETWEEN INTEGRATED TRAJECTORIES AND FLUID TRAJECTORIES

At longer integration times in these chaotic flows, small inaccuracies in the velocity field can lead to large deviations between virtual particle trajectories and the trajectories of the rods. We can correct for the deviations of virtual particle trajectories from rods by forcing the center of a group of virtual particles to follow the center of a rod. This way, we are sampling the same stretching that the rod has experienced. Figure 12 shows the effect of forcing the virtual particles to follow the rods on the probability distribution of alignment of rods with the direction of past stretching. The distribution in Fig. 12(a) shows that the benefit of forcing the virtual particles to follow the rods is quite small. However, if we only look at rods that experience large stretching [Fig. 12(b)], the effect of forcing the virtual particles to follow the rods is to create a significantly stronger alignment. We conclude that integration errors can have some effect in regions of large stretching, but the overall effect on the orientation distributions we measure is not significant. We also performed this analysis on the data from the nonperiodic experiment. Here, forcing the particles to follow the rods led to somewhat worse alignment in some cases. We interpret this as a result of the fact that in the nonperiodic experiment, there can never be velocity tracer particles at the position of the rods. Forcing the virtual particles to follow the rods in this case can force them into regions where the velocity field is not resolved as accurately.

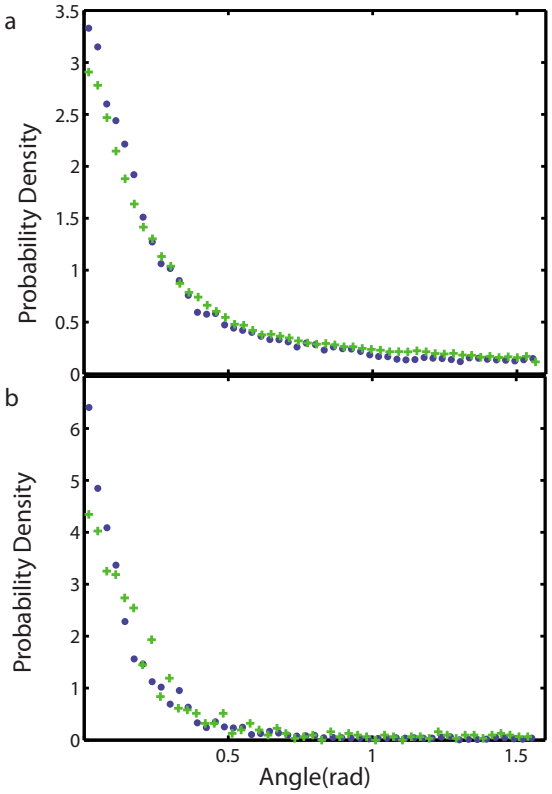

FIG. 12. (Color online) PDF of alignment of rods with the direction of stretching, showing the effect of forcing virtual particles to follow the trajectories of rods. Data are for the periodic flow with 10 mm rod length and integration time ($\Delta t = T$). (a) Probability distribution calculated for all stretching values; (b) probability distribution conditioned for stretching values larger than one rms. ● virtual particles follow the rod trajectory, + virtual particle trajectory may deviate from rod trajectory.

[1] F. Toschi and E. Bodenschatz, "Lagrangian properties of particles in turbulence," Annu. Rev. Fluid Mech. **41**, 375 (2009).
[2] N. M. Qureshi, M. Bourgoin, C. Baudet, A. Cartellier, and Y. Gagne, "Turbulent transport of material particles: An experimental study of finite size effects," Phys. Rev. Lett. **99**, 184502 (2007).
[3] N. T. Ouellette, P. J. J. O'Malley, and J. P. Gollub, "Transport of finite-sized particles in chaotic flow," Phys. Rev. Lett. **101**, 174504 (2008).
[4] R. D. Brown, Z. Warhaft, and G. A. Voth, "Acceleration statistics of neutrally buoyant spherical particles in intense turbulence," Phys. Rev. Lett. **103**, 194501 (2009).
[5] J. A. Olson and R. J. Kerekes, "The motion of fibres in turbulent flow," J. Fluid Mech. **377**, 47 (1998).
[6] C. P. R. Saunders, "Thunderstorm electrification laboratory experiments and charging mechanisms," J. Geophys. Res. **99**, 10773, doi:10.1029/93JD01624 (1994).
[7] C. P. R. Saunders, S. L. Peck, G. G. Aguirre Varela, E. E. Avila, and N. E. Castellano, "A laboratory study of the influence of water vapour and mixing on the charge transfer process during collisions between ice crystals and graupel," Atmos. Res. **58**, 187 (2001).
[8] S. C. Sherwood, V. T. J. Phillips, and J. S. Wettlaufer, "Small ice crystals and the climatology of lightning," Geophys. Res. Lett. **33**, L05804, doi:10.1029/2005GL025242 (2006).
[9] M. B. Pinsky and A. P. Khain, "Some effects of cloud turbulence on water-ice and ice-ice collisions," Atmos. Res. **47–48**, 69 (1998).
[10] G. B. Jeffery, "The motion of ellipsoidal particles immersed in a viscous fluid," Proc. R. Soc. London, Ser. A **102**, 161 (1922).
[11] G. I. Taylor, "The motion of ellipsoidal particles in a viscous fluid," Proc. R. Soc. London, Ser. A **103**, 58 (1923).

[12]H. Brenner, "The Stokes resistance of an arbitrary particle," Chem. Eng. Sci. **18**, 1 (1963).
[13]H. Brenner, "The Stokes resistance of an arbitrary particle—II. An extension," Chem. Eng. Sci. **19**, 599 (1964).
[14]H. Brenner, "The Stokes resistance of an arbitrary particle—III. Shear fields," Chem. Eng. Sci. **19**, 631 (1964).
[15]H. Brenner, "The Stokes resistance of an arbitrary particle—IV. Arbitrary fields of flow," Chem. Eng. Sci. **19**, 703 (1964).
[16]E. Gavze and M. Shapiro, "Motion of inertial spheroidal particles in a shear flow near a solid wall with special application to aerosol transport in microgravity," J. Fluid Mech. **371**, 59 (1998).
[17]G. Subramanian and D. L. Koch, "Inertial effects on fibre motion in simple shear flow," J. Fluid Mech. **535**, 383 (2005).
[18]A. J. Szeri, S. Wiggins, and L. G. Leal, "On the dynamics of suspended microstructures in unsteady, spatially inhomogeneous, 2-dimensional fluid flows," J. Fluid Mech. **228**, 207 (1991).
[19]A. J. Szeri, W. J. Milliken, and L. G. Leal, "Rigid particles suspended in time-dependent flows: irregular versus regular motion, disorder versus order," J. Fluid Mech. **237**, 33 (1992).
[20]A. J. Szeri and L. G. Leal, "Microstructure suspended in 3-dimensional flows," J. Fluid Mech. **250**, 143 (1993).
[21]A. J. Szeri, "Pattern-formation in recirculating-flows of suspensions of orientable particles," Philos. Trans. R. Soc. London, Ser. A **345**, 477 (1993).
[22]S. S. Girimaji and S. B. Pope, "Material element deformation in isotropic turbulence," J. Fluid Mech. **220**, 427 (1990).
[23]E. Dresselhaus and M. Tabor, "The kinematics of stretching and alignment of material elements in general flow fields," J. Fluid Mech. **236**, 415 (1992).
[24]P. H. Mortensen, H. I. Andersson, J. J. J. Gillissen, and B. J. Boersma, "On the orientation of ellipsoidal particles in a turbulent shear flow," Int. J. Multiphase Flow **34**, 678 (2008).
[25]P. H. Mortensen, H. I. Andersson, J. J. J. Gillissen, and B. J. Boersma, "Dynamics of prolate ellipsoidal particles in a turbulent channel flow," Phys. Fluids **20**, 093302 (2008).
[26]M. Shin and D. L. Koch, "Rotational and translational dispersion of fibres in isotropic turbulent flows," J. Fluid Mech. **540**, 143 (2005).
[27]M. Wilkinson, V. Bezuglyy, and B. Mehlig, "Fingerprints of random flows?" Phys. Fluids **21**, 043304 (2009).
[28]C. M. Zettner and M. Yoda, "Moderate-aspect-ratio elliptical cylinders in simple shear with inertia," J. Fluid Mech. **442**, 241 (2001).
[29]K. B. Moses, S. G. Advani, and A. Reinhardt, "Investigation of fiber motion near solid boundaries in simple shear flow," Rheol. Acta **40**, 296 (2001).
[30]R. Holm and D. Soderberg, "Shear influence on fibre orientation–Dilute suspension in the near wall region," Rheol. Acta **46**,721 (2007); Third Annual European Rheology Confererence, Hersonissos, Greece, 27–29 April 2006.
[31]M. Parsheh, M. L. Brown, and C. K. Aidun, "Variation of fiber orientation in turbulent flow inside a planar contraction with different shapes," Int. J. Multiphase Flow **32**, 1354 (2006).
[32]O. Bernstein and M. Shapiro, "Direct determination of the orientation distribution function of cylindrical particles immersed in laminar and turbulent shear flows," J. Aerosol Sci. **25**, 113 (1994).
[33]R. K. Newsom and C. W. Bruce, "Orientational properties of fibrous aerosols in atmospheric turbulence," J. Aerosol Sci. **29**, 773 (1998).
[34]L. E. Malvern, *Introduction to the Mechanics of a Continuous Medium* (Prentice-Hall, London, 1969).
[35]G. Haller and G. Yuan, "Lagrangian coherent structures and mixing in two-dimensional turbulence," Physica D **147**, 352 (2000).
[36]G. A. Voth, G. Haller, and J. P. Gollub, "Experimental measurements of stretching fields in fluid mixing," Phys. Rev. Lett. **88**, 254501 (2002).
[37]M. Mathur, G. Haller, T. Peacock, J. E. Ruppert-Felsot, and H. L. Swinney, "Uncovering the Lagrangian skeleton of turbulence," Phys. Rev. Lett. **98**, 144502 (2007).
[38]M. J. Twardos, P. E. Arratia, M. K. Rivera, G. A. Voth, J. P. Gollub, and R. E. Ecke, "Stretching fields and mixing near the transition to nonperiodic two-dimensional flow," Phys. Rev. E **77**, 056315 (2008).
[39]Independent but complementary experiments for periodic and nonperiodic flows were performed using similar apparatuses by groups at Wesleyan and Haverford, respectively, which accounts for the slight differences in materials and procedures for the two types of flows.
[40]D. Vella and L. Mahadevan, "The 'Cheerios effect'," Am. J. Phys. **73**, 817 (2005).
[41]N. T. Ouellette, H. Xu, and E. Bodenschatz, "A quantitative study of three-dimensional Lagrangian particle tracking algorithms," Exp. Fluids **40**, 301 (2006).
[42]A. J. Szeri and L. G. Leal, "A new computational method for the solution of flow problems of microstructured fluids. Part 1. Theory," J. Fluid Mech. **242**, 549 (1992).